Numerical aspects of an algorithm for the eulerian simulation of two-phase flows

— **Source link** ↗

Paulo J. Oliveira, R. I. Issa

Institutions: University of Beira Interior, Imperial College London

Related papers:

- Thermo-fluid dynamic theory of two-phase flow

- Computational fluid dynamics of dispersed two-phase flows at high phase fractions

- Numerical heat transfer and fluid flow

- Solution of the implicitly discretised reacting flow equations by operator-splitting

- Modelling of dispersed bubble and droplet flow at high phase fractions

NUMERICAL ASPECTS OF AN ALGORITHM FOR THE EULERIAN SIMULATION OF TWO-PHASE FLOWS

Paulo J. Oliveira[*] and Raad I. Issa[†]

[*]Departamento de Engenharia Electromecânica
Universidade da Beira Interior, 6200 Covilhã, Portugal.

[†]Department of Mechanical Engineering
Imperial College of Science, Technology and Medicine, London SW7 2BX, UK.

Key words: Two-phase Flow, Numerical Method, Eulerian Formulation

Abstract. *It is often the case that the numerical simulation of two phase flows leads to a number of difficulties associated with the solution algorithms utilized. Those difficulties manifest themselves as an impossibility to converge the iterative solution process, typical of the finite-volume pressure-correction methods, and are particularly persistent in cases with phase segregation (complete, or almost complete, separation of one phase from the other) and with fine meshes. A number of effective measures to overcome such problems are here proposed and tested, encompassing: (1) modification of the momentum equations formulation in a way that avoids singularity as volume fractions tend to zero; (2) bounding of the volume fractions during the iterative algorithm in a way that enforces the physical limits, $\alpha \geq 0$ and $\alpha \leq 1$; (3) symmetric treatment of some terms in the equations, and consistent formulation of cell-face fluxes in order to prevent numerical-induced oscillations.*

1

1 INTRODUCTION

Numerical modelling of two phase flows using the Eulerian approach is one in which both phases are treated as interpenetrating continua and suitably averaged momentum equations are solved for both[1]. In this study we examine, from a numerical perspective, the behaviour of a typical finite-volume algorithm for the solution of the Eulerian equations for two phase flow. By "typical" we mean pressure-based, iterative algorithms similar to that described in previous work[2], which in many ways descends from the early IPSA algorithm of Spalding[3]. Recent representative applications of that type of algorithm are given in the work of refs.[4,5].

Experience with iterative two-phase flow algorithms (for example[2]) has invariably led to numerical problems, especially when there is segregation of the phases or when recirculation zones occur. In practical terms the outcome is the impossibility to converge the iterative-like procedure used to solve the sets of discretized equations. Often convergence is hindered due to the inability to solve the equations to the prescribed tolerance in only a few problematic cells of the mesh, but the solution is otherwise achieved in most of the computational domain. Lack of robustness is also observed when the computational grid is refined.

The purpose of this work is to investigate some of the key numerical issues which affect the robustness of two-phase algorithms and to devise and test various procedures designed to improve algorithm performance. In particular, the following issues have been studied:

• Behaviour of the velocity field for each phase as the volume fractions go to zero. The standard formulation for the momentum equations become singular in that limit, so the resulting velocities can fluctuate widely in the regions where volume fractions tend to vanish. This causes numerical problems, especially at the boundary between regions of segregated phases.

• Boundedness of the volume fraction field, especially as the volume fraction tends to one of its physical limits (zero or one). This issue is related to the choice of equations solved to obtain the volume fractions, as will be discussed in the paper.

• Behaviour of the algorithm with mesh refinement. One of the important requirements of a generally applicable algorithm is "robustness", when fine computational meshes are used to obtain numerically resolved solutions.

• Capability of the algorithm to handle phase segregation.

The proposed remedies have been tested and verified for several test cases which exhibit the flow features above and the results of these tests are presented.

2 DIFFERENTIAL EQUATIONS

In this section the standard form of the averaged momentum equations comprising the Eulerian two-fluid model for two-phase flows are given first, and then the steps required to obtain a working set of equations, after division of each by its volume-fraction, are explained. The final form of the governing equations are listed at the end of the section.

2.1 Basic governing equations

The basic averaged equations are those representing conservation of mass and momentum for each phase k (c for continuous and d for dispersed):

$$\frac{\partial}{\partial t}\alpha_k + \nabla \cdot \alpha_k u_k = 0 \tag{1}$$

$$\frac{\partial}{\partial t}\rho_k\alpha_k u_k + \nabla \cdot \rho_k\alpha_k u_k \otimes u_k = \nabla \cdot \alpha_k T_k + \rho_k\alpha_k g + M_k \tag{2}$$

The averaging procedure and the resulting equations are by now relatively well established[1] although some differences may arise due to the detailed treatment of the interphase terms. In Eqs. (1) and (2) u is a phase averaged velocity, α is a volume fraction, and both phases are assumed to have a constant density ρ. The total stress tensor is decomposed into an isotropic pressure term and an effective (molecular + turbulent) deformation stress as:

$$T_k = -p_k\,\delta + \tau_k \tag{3}$$

The interface momentum transfer term can be decomposed into drag, virtual mass and an interface-average stress contribution, denoted by a corresponding superscript, as:

$$M_k = M_k^D + M_k^{VM} + M_k^I \tag{4}$$

with

$$M_k^D = C_f[\alpha_k\hat{\alpha}_k(\hat{u}_k - u_k) - \eta_k\nabla\alpha_k] \quad (C_f = \tfrac{3}{4}\frac{\rho_c C_D u_r}{d_p} = \frac{18\mu_c f}{d_p^2}) \tag{5}$$

$$M_k^{VM} = \rho_c C_{VM}\alpha_k\hat{\alpha}_k(\frac{\mathrm{D}\hat{u}_k}{\mathrm{D}t} - \frac{\mathrm{D}u_k}{\mathrm{D}t}) \tag{6}$$

$$M_k^I = \int_{A_i} T_{ki} \cdot n_k\,\mathrm{d}a = -T_{ki} \cdot \nabla\alpha_k = p_{ki}\,\nabla\alpha_k - \tau_{ki} \cdot \nabla\alpha_k \tag{7}$$

where the symbol ^ denotes the other phase. Other interface forces are known to arise and be significant in some circumstances, such as lift or history forces, but their effect on the numerical behaviour of the algorithm has not been considered here. Furthermore, since the objective was to study numerical aspects of the solution procedure, simple models have been used for the phasic interactions, although they assume the usual forms which lead to numerical difficulties. The drag was assumed to follow the standard curve for drag around a sphere of diameter d_p, namely $C_D = (24/\mathrm{Re}_p)f(\mathrm{Re}_p)$ with $f = 1 + 0.15\,\mathrm{Re}_p^{0.687}$ and $\mathrm{Re}_p = \rho_c u_r d_p/\mu_c$. Also[6,7], the instantaneous drag gives rise to a turbulent drag term, proportional to the eddy diffusivity ($\eta_k = \nu_k^t/\sigma_\alpha$ with $\sigma_\alpha = 0.71$) in Eq. (5).

2.2 Alternative form of the equations

As mentioned earlier, in the limit of $\alpha_k \rightarrow 0$, the momentum equation for phase k becomes singular. Division of the momentum equations by α_k lead to well-behaved velocity fields in the limit of vanishing velocity of the other phase; in the absence of flow-induced accelerations, the velocity of either phase will then tend to the corresponding "terminal velocity". If the momentum equations (2) are expressed in non-conservative form (by differentiating the convection terms) and then divided by α_k we obtain:

$$\rho_k \frac{\mathrm{D}\boldsymbol{u}_k}{\mathrm{D}t} = -\nabla p_k + \nabla \cdot \tau_k' - \tfrac{2}{3}\rho_k \nabla \mathrm{k}_k + \rho_k \boldsymbol{g} - K_k \frac{\nabla \alpha_k}{\alpha_k} + \hat{\alpha}_k C_f (\hat{\boldsymbol{u}}_k - \boldsymbol{u}_k) +$$

$$+ \ \hat{\alpha}_k \rho_c C_{vm} (\frac{\mathrm{D}\hat{\boldsymbol{u}}_k}{\mathrm{D}t} - \frac{\mathrm{D}\boldsymbol{u}_k}{\mathrm{D}t})$$

(8)

where

$$K_k = -(p_{ki} - p_k) + C_f \eta_k.$$

(9)

In Eq. (8) it is assumed that $\tau_k = \tau_{ki}$, but a difference between the average phase stress and its interfacial average could be included. The effective stress is linearly related to the strain rate via a Boussinesq relationship, with the effective viscosity being the sum of molecular and turbulent contributions (to be obtained from the k-ϵ turbulence model). In arriving at Eq. (8) the stress was decomposed as:

$$\tau_k = \tau_k' - \tfrac{2}{3}\rho_k \mathrm{k}_k \ \delta$$

(10)

with

$$\tau_k' = \mu_k^{ef} (\nabla \boldsymbol{u}_k + \nabla \boldsymbol{u}_k^T - \tfrac{2}{3}\nabla \cdot \boldsymbol{u}_k \ \delta)$$

(11)

The normal turbulent stress is written separately (using the stress deviator τ') because it is an important factor for phase dispersion and may be subjected to specific numerical treatment.

It is noted that the simplifications leading to Eq. (8) were possible because the interface forces (drag, Eq. (5), and virtual mass, Eq. (6)) were assumed to be proportional to the product of both volume fractions, $\alpha_k \hat{\alpha}_k$. Not all authors make that assumption, but there are physical arguments to justify it. A consequence of the present manipulation is that the only problematic term remaining, when $\alpha_k \rightarrow 0$, is the interface term being proportional to $\nabla \alpha / \alpha$. It is required that the gradient of α goes to zero faster than α, as $\alpha \rightarrow 0$.

2.3 Special symmetric treatment of terms

In arriving at the final form of the momentum equations, from Eq. (8), two terms deserve special attention so that the resulting equations remain symmetric in relation to either phase. We deal first with the gravity term and then with the normal stress term.

It will generally be assumed that the same static pressure acts in both phases, $p_k = p$. The gravity terms in the above equations are usually written in terms of a buoyancy term

appearing solely in the dispersed phase equation, after subtracting the weight of the continuos phase from the static pressure. This manipulation leads to modified pressure gradient and body-force terms of the form (prior to division by the volume fraction):

continuous phase: $-\alpha_c \nabla \tilde{p}$

dispersed phase: $-\alpha_d \nabla \tilde{p} - \alpha_d \boldsymbol{g}\, \Delta\rho$ (with $\Delta\rho = \rho_c - \rho_d$)
$\hspace{10cm}$ (12)

where $\tilde{p} = p - \rho_c g\, y + \text{constant}$ (y is the direction vertically upwards and g is the magnitude of gravity). When there is no reason to treat one of the phases differently from the other, such as in separated flow regimes (stratified flow, for example), it is better to use a symmetric treatment and define the modified pressure as:

$$\nabla \tilde{p} = \nabla p - g\rho_m \quad (\text{with } \rho_m = \alpha_c \rho_c + \alpha_d \rho_d) \tag{13}$$

A manipulation similar to that above leads now to modified pressure gradient and body-force terms of the form (prior to division by the volume fraction):

continuous phase: $-\alpha_c \nabla \tilde{p} + \alpha_d \alpha_c \boldsymbol{g}\, \Delta\rho$

dispersed phase: $-\alpha_d \nabla \tilde{p} - \alpha_d \alpha_c \boldsymbol{g}\, \Delta\rho$
$\hspace{10cm}$ (14)

The advantage of this new modified pressure is that $\tilde{p}$ will not suffer any change of slope across a stratified flow.

In what relates to the turbulent normal stress term (the $2/3\rho\nabla k$ terms in Eq. 8), they can be included into a modified pressure in a symmetric way similar to that for the gravity terms above. The original momentum equation has terms of the form:

$$-\alpha_k \nabla p - \tfrac{2}{3}\alpha_k \rho_k \nabla k_k$$

where it is assumed that the densities ρ_k are constant. Define the modified pressure as:

$$\nabla \tilde{p} = \nabla p + \tfrac{2}{3}(\alpha_c \rho_c \nabla k_c + \alpha_d \rho_d \nabla k_d) \tag{15}$$

where the turbulent kinetic energies of the continuous and dispersed phases are k_c and k_d, respectively. These are related to each other in the turbulence model employed in this work by $k_d = C_k k_c$. Then the relevant terms in the equations become:

continuous phase: $-\alpha_c \nabla \tilde{p} - \alpha_d \alpha_c \tfrac{2}{3}\nabla(\rho_c k_c - \rho_d k_d)$

dispersed phase: $-\alpha_d \nabla \tilde{p} + \alpha_d \alpha_c \tfrac{2}{3}\nabla(\rho_c k_c - \rho_d k_d)$
$\hspace{10cm}$ (16)

2.4 Final equations

After inserting the symmetric treatment just explained for the gravity and normal stress into the momentum equations, we arrive at the following working form of the various governing equations.

Momentum equation for the continuous phase

$$
\rho_c \frac{D\boldsymbol{u}_c}{Dt} = -\nabla p + \nabla \cdot \tau'_c - \tfrac{2}{3}\alpha_d \nabla\big(\rho_c \mathrm{k}_c - \rho_d \mathrm{k}_d\big) + \alpha_d \boldsymbol{g}\, \Delta\rho + K_c \frac{\nabla\alpha_d}{\alpha_c} +
$$
$$
+ \alpha_d C_f(\boldsymbol{u}_d - \boldsymbol{u}_c) + \alpha_d \rho_c C_{vm}\big(\frac{D\boldsymbol{u}_d}{Dt} - \frac{D\boldsymbol{u}_c}{Dt}\big) \tag{17}
$$

Momentum equation for the dispersed phase:

$$
\rho_d \frac{D\boldsymbol{u}_d}{Dt} = -\nabla p + \nabla \cdot \tau'_d + \tfrac{2}{3}\alpha_c \nabla\big(\rho_c \mathrm{k}_c - \rho_d \mathrm{k}_d\big) - \alpha_c \boldsymbol{g}\, \Delta\rho - K_d \frac{\nabla\alpha_d}{\alpha_d} +
$$
$$
+ \alpha_c C_f(\boldsymbol{u}_c - \boldsymbol{u}_d) + \alpha_c \rho_c C_{vm}\big(\frac{D\boldsymbol{u}_c}{Dt} - \frac{D\boldsymbol{u}_d}{Dt}\big) \tag{18}
$$

with: $K_c = K_d = C_f \nu^t/\sigma_\alpha$ (here it is assumed that $p_{ki} = p_k$) .

Continuity equation for the continuous phase:

$$
\frac{\partial}{\partial t}\alpha_c + \nabla \cdot \alpha_c u_c = 0 \tag{19}
$$

Continuity equation for the dispersed phase:

$$
\frac{\partial}{\partial t}\alpha_d + \nabla \cdot \alpha_d u_d = 0 \tag{20}
$$

Equation of phase compatibility:

$$
\alpha_c + \alpha_d = 1 \tag{21}
$$

Turbulence modelling is not the issue under study here, hence the equations governing the transport of turbulent kinetic energy ($\mathrm{k} = \mathrm{k}_c$) and its dissipation rate ($\epsilon = \epsilon_c$)[6,7] are merely stated below. They are:

$$
\rho_c \frac{D\mathrm{k}}{Dt} = \nabla \cdot \frac{\mu^t}{\sigma_\mathrm{k}}\nabla\mathrm{k} + (\mathrm{G} - \rho_c\epsilon) + S_\mathrm{k} \tag{22}
$$

$$
\rho_c \frac{D\epsilon}{Dt} = \nabla \cdot \frac{\mu^t}{\sigma_\epsilon}\nabla\epsilon + \tfrac{\epsilon}{\mathrm{k}}(\mathrm{C}_1\mathrm{G} - \mathrm{C}_2\rho_c\epsilon) + S_\epsilon \tag{23}
$$

where the source terms are:

$$S_{\mathrm{k}} = 2k\alpha_d C_f(C_{\mathrm{i}} - 1) \;+\; C_f \frac{\nu^t}{\sigma_\alpha} \frac{\nabla\alpha_d}{\alpha_c} \cdot \boldsymbol{u}_r \quad \text{(mean slip velocity, } \boldsymbol{u}_r = \boldsymbol{u}_d - \boldsymbol{u}_c) \qquad (24)$$

for the kinetic energy, and

$$S_\epsilon = 2C_3\epsilon\alpha_d C_f(C_{\mathrm{i}} - 1) \qquad (25)$$

for the dissipation rate, and where $C_{\mathrm{i}} = \overline{u'_d \cdot u'_c} \;/\overline{u'_c \cdot u'_c}$ (covariance or interaction coefficient). It is noted that the $(C_{\mathrm{i}} - 1)$-term in these dispersed-phase-related terms should be treated implicitly if $C_{\mathrm{i}} < 1$ (case of solid particles in a gas); otherwise (gas bubbles in a liquid, $C_{\mathrm{i}} > 1$), it should be left on the right-hand-side of the equations. The dispersed phase turbulent kinetic energy and viscosity are related to the continuous phase ones by means of response functions:

$$k_d = C_{\mathrm{k}} \, k_c \quad \text{and} \quad \nu_d^t = C_\nu \, \nu_c^t$$

with:

$$\nu_c^t = C_\mu k_c/\epsilon, \quad \mu_c^{ef} = \mu_c + \rho_c\nu_c^t \quad \text{and} \quad \mu_d^{ef} = \rho_d(\nu_{\mathrm{d}} + \nu_d^t).$$

In this work we have used $C_\nu = 1$, $C_{\mathrm{i}} = 1$, $C_3 = 0$ (no turbulent modulation terms) and C_{k} followed an expression given by ref. 6:

$$C_{\mathrm{k}} = C_{\mathrm{t}}^2, \text{ with } C_{\mathrm{t}} = \frac{3+\beta}{1+\beta+2\rho_{\mathrm{d}}/\rho_{\mathrm{c}}} \;, \quad \beta = \frac{t_\epsilon}{t_p}\left(1 + 2\frac{\rho_d}{\rho_c}\right)$$

where t_ϵ is a time scale of the large eddies (typically $t_\epsilon = C_\epsilon k/\epsilon$, with $C_\epsilon = 0.4$) and t_p is the "particle" relaxation time ($t_p = (\rho_d/C_f)(1 + C_{vm}\rho_c/\rho_d)$, with $C_{vm} = 0.5$).

3 DISCRETISED EQUATIONS

In this section the discretised form of the governing equations, which is based on a standard finite-volume method, is given. The methodology developed to ensure that the volume fractions remain bounded is then presented. This is a key point of the work and one that has received little attention in the past, albeit being essential to ensure robustness of the numerical method.

3.1 Momentum equations and fluxes

A non-staggered mesh arrangement is utilised, following previous work[2]. All variables are stored at the centre of the control volumes over which the governing equations are

integrated, resulting in sets of linearised algebraic equations of the form[8,9] $a_P\phi_P = H(\phi) + S_\phi$ which are then solved with conjugate gradient methods for linear-equation sets. The discretised cell-centered momentum equations, with implicit treatment of drag and virtual mass, is written in simplified 1-D fashion as:

$$a_P u_P = H(u) - B_P[\Delta p]_P - V_P K_P \frac{[\Delta\alpha]_P}{\alpha_P} + \hat{\alpha}_P C_f \hat{u}_P V_P +$$

$$+ (\frac{\rho'V}{\delta t})_P u_P^0 + S_u + \rho_c \hat{\alpha}_P C_{vm} \sum_F \hat{a}_F^C (\hat{u}_P - \hat{u}_F) \tag{26}$$

with

$$a_P = \sum_F a_F + (\frac{\rho'V}{\delta t})_P + \hat{\alpha}_P C_f V_P$$

$$a_F = a_F^D + a_F^C \quad \text{(diffusion and } VM\text{-corrected convection contributions)} \tag{27}$$

$$H(u) = \sum_F a_F u_F.$$

In these equations, $\rho' \equiv \rho(1 + \hat{\alpha} C_{vm}\rho_c/\rho)$ is an effective density corrected for virtual mass effects, P is the cell in question, F are the neighbouring cells (6 in a general 3D problem, 4 in 2D), and S_u is the source term containing all contributions not explicitly written (such as buoyancy and normal turbulent stress terms, for example). Note the conservative and consistent formulation of the virtual-mass term, based on the convective coefficients of the other phase (here evaluated with volumetric flow rates). V_P is the volume of a cell, B_P are cell surface areas and δt the time step.

Convection fluxes at a cell face (f, between P and F) are evaluated with face velocities $\tilde{u}_f$ defined from a a special Rhie-Chow interpolation practice[2], as:

$$\overline{a_P}\,\tilde{u}_f = \overline{H(u)} - B_f[\Delta p]_f - V_f\overline{K}_f\frac{[\Delta\alpha]_f}{\alpha_P} + \overline{\hat{\alpha}}_f\overline{C_f}\,\tilde{u}_f V_f + \overline{(\frac{\rho'V}{\delta t})}_f\tilde{u}_f^0 + \overline{S_u} \tag{28}$$

where the overbar denotes arithmetic average; the virtual-mass term is embedded into the source term. Note that the gradient of α is evaluated directly at the cell face f (and not by averaging) and thus oscillations in α will be avoided.

3.2 Bounding of α and the various forms of the continuity equation

The volume fractions are obtained from solution of one of the continuity equations, either Eq. (19) or (20). The important question is how to ensure boundedness of α, i.e. $0 \le \alpha_k \le 1$ for $k = c$ or $k = d$. Early studies of this issue are found in Carver[10].

3.2.1 Standard method

One of the continuity equations, typically that for the dispersed phase Eq. (20), is discretised and solved as a transport equation for $\alpha \equiv \alpha_d$. This equation is written in the linearised form:

$$a_P^\alpha \, \alpha_P \; = \; H^\alpha(\alpha) \; + \; S_\alpha \tag{29}$$

with coefficients and source terms given by:

$$H^\alpha(\alpha) \; = \sum_F a_F^\alpha \, \alpha_F \qquad a_{F+}^\alpha = \; - \, f_{f+}^- \qquad a_{F-}^\alpha = \; + \, f_{f-}^+ \quad (f^+ \equiv \mathrm{Max}(f,0), \, f^- \equiv \mathrm{Min}(f,0))$$

$$a_P^\alpha \; = \; \sum_F a_F^\alpha \; + \; \frac{\rho V}{\delta t} \; + \; (\nabla \cdot u)^+ \tag{30}$$

$$S^\alpha \; = \; - \, (\nabla \cdot u)^- \alpha_P^0 \; + \; \frac{V}{\delta t} \, \alpha_P^0$$

A positive cell neighbour or face is here denoted F^+ or f^+ (e.g. east, north and top), and a negative cell neighbour and face by F^- and f^- (e.g. west, south and bottom). The upwind scheme is used to represent the convective fluxes "f" (higher order methods are also possible). The other volume fraction is then obtained from Eq. (21), $\alpha_c = 1 - \alpha_d$. A consequence of upwinding is that all coefficients in Eq. (30) are positive so this method guarantees that α_d is bounded by zero ($\alpha_d \geq 0$) but does not guarantee boundedness by 1.

3.2.2 Two-equation method

With this approach both phase continuity equations are solved separately for the two phase fractions. Since it is easy to bound both volume fractions from below ($\alpha_d \geq 0$ and $\alpha_c \geq 0$) using the standard discretisation schemes with the upwind scheme, and since $\alpha_d + \alpha_c = 1$, then both α_d and α_c will be bounded by 1 at convergence. In order to exactly enforce this constraint, the volume fractions obtained from solution of Eqs. (19) and (20), denoted α_d^* and α_c^*, are corrected by a factor $\mathfrak{f}$ as:

$$\alpha_d \; = \; \mathfrak{f} \, \alpha_d^* \quad \text{and} \quad \alpha_c \; = \; \mathfrak{f} \, \alpha_c^* \tag{31}$$

Now, since $\alpha_d + \alpha_c = 1$, hence:

$$\mathfrak{f} \; = \; 1/(\alpha_d^* + \alpha_c^*). \tag{32}$$

Spalding[3] used a similar correction in early developments of his IPSA method but appear to have abandoned it later. A minor point against this method is that it requires solution of two continuity equations. However, due to upwinding, these equations are extremely easy to solve and often one iteration of the CGS solver is sufficient to reduce the initial residuals to below 0.5%. A second point is that the process is iterative in nature with convergence only

attained as $f \to 1$. This is not an issue in steady state calculations where iteration is utilised, and is only a consideration in time-dependent applications.

4 RESULTS

The reformulated momentum equations of section 2 and the new method for obtaining the volume fractions discussed in section 3 have been implemented in a computer code. This code is the same used in previous work[2] and is based on the finite-volume method in non-staggered meshes. We can then compare the numerical behaviour of the "new" against the "old" formulation[2], especially in terms of convergence rate, robustness with mesh refinement, and capacity to handle a wide range of volume fractions in a given problem. The following three test cases have been considered:

(1) Turbulent bubbly flow in an axisymmetric sudden expansion
(2) Turbulent high-void fraction bubbly flow about a plane obstruction
(3) Stratified laminar flow in a channel

4.1 Sudden expansion

The relevant dimensions for this problem were $R_1 = 25$mm, $R_2 = 50$mm (expansion ratio $R_2/R_1 = 2$), inlet pipe length $L_1 = 25$mm and outlet pipe length $L_2 = 350 + 1000 = 1350$mm. The flow was turbulent, with $\mathrm{Re} = \rho_c 2 R_1 \bar{u}_{c1}/\mu_c \approx 10^5$, and the inlet profiles were obtained from the measurements of Bel Fdhila[11]. The average value of the void fraction α at inlet was $\approx 5\%$ and the bubble diameter $d_p = 2$mm.

Mesh refinement - Three meshes have been utilised, refined consistently (mesh doubling) along both the axial and radial directions. Since the mesh is non-uniform in the axial direction with higher concentration of cells closer to the expansion plane, doubling the mesh requires taking the square-root of the geometrical expansion factors used to distribute the mesh spacing ($f_x \equiv \delta x_{i+1}/\delta x_i$). In this way, the minimum spacing in a zone of non-uniform mesh is effectively halved when going from a coarser to a finer mesh. The mesh characteristics are given in Table 1, where f_x refers to the mesh blocks (length 350 mm) just downstream of the expansion plane.

An idea of the finer mesh (mesh-3) can be obtained from Fig. 1, where contours of the predicted void fraction (α) and turbulent kinetic energy (normalised by its maximum value) are also given, together with the mixture streamlines. Fig. 1 shows agglomeration of the gas phase in the main part of the recirculating zone, where the turbulent kinetic energy also shows its highest levels. The region just behind the step-wall is devoid of gas bubbles ($\alpha \approx 0$).

mesh	NC	$\delta x_{\min}/R_1$	f_x	f_r
1	2200	0.1	1.01560	1.0
2	8800	0.05	1.00770	1.0
3	35200	0.025	1.00384	1.0

Table 1.: Meshes used for the sudden expansion case (NC: number of cells).
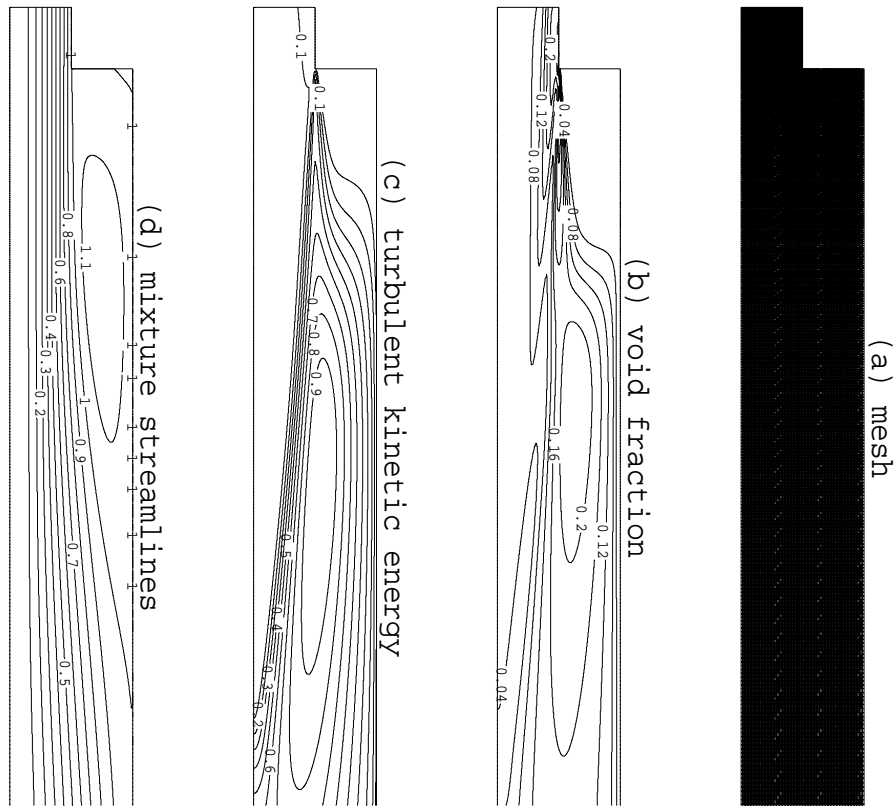
Figure 1 Predictions for the sudden expansion flow: (a) Mesh, (b) void fraction contours, (c) turbulent kinetic energy contours, and (d) mixture streamlines.

The effect of mesh refinement upon the predicted profiles of void fraction is shown in Fig. 2. There is good convergence with mesh refinement except for the profile closer to the expansion plane ($x = 70$mm) where larger differences are seen in the predictions with the coarser mesh (the local maximum of α at $r/R_1 \approx 0.7$ is due to the imposed inlet profile).

New and old formulation - The main differences between the two is the division of the momentum equations by α and the inclusion of the virtual mass term. The division by α implies some difference on the stress terms (due to the approximation $\tau_k = \tau_{ki}$; compare Eq. 2 with Eq. 8). In terms of the method used to obtain α, the "old method" uses the standard method (section 3.2.1) while the "new method" can use either of two methods (sections 3.2.1 and 3.2.2) for solving the α-equation.

For the predictions in the coarser mesh, Fig. 3 shows the decay of the u-momentum residuals as time-marching proceeds (the behaviour of the other variables is similar). The figure compares the residuals' history with the two methods, and also with the old method when the turbulent-drag term in the dispersed phase momentum equation is switched off (second term in Eq. 5). Clearly, when this term is present the "old" method cannot converge to the specified tolerance (here 10^{-4}) but by switching it off convergence can be achieved.
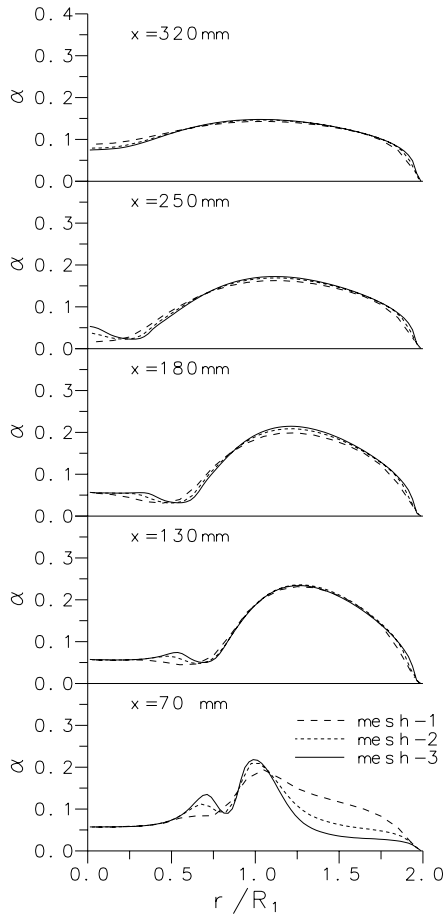
11

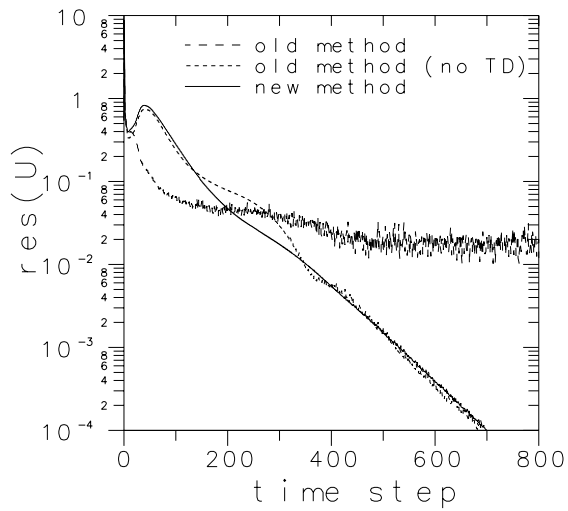Figure 2 Effect of mesh refinement on the void fraction profiles.

Figure 3 Decay of the residuals with the "old" and the "new" method (TD: turbulent drag).

In the "new" method all terms are present. This problem was traced back to the relative velocity which attains unphysical high values just inside the area where $\alpha_d \approx 0$ because the momentum equation is then singular (or undefined $0 = 0$). For this case the problem is restricted to a few problematic cells in that area.

A few comparison of volume fraction profiles obtained with the new and old methods (using the same method for α) are shown in Fig. 4. The differences seen in the figure are a result of the approximation $\tau_k = \tau_{ki}$; they are small and only become significant close to the expansion plane. The fact that these results were obtained on the coarser mesh presumably tends to accentuate those differences.

Bounding of volume fraction and method used to solve for α - In terms of accuracy, Fig. 5 shows three typical radial profiles of α predicted on mesh-2 with the standard and the two-equation method; both give essentially the same results.
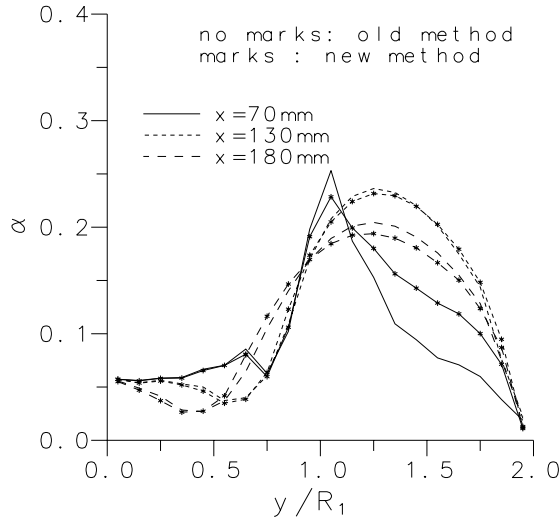
Figure 4: Comparison of 3 void fraction profiles predicted in the coarse mesh with the "new" and the "old" method.
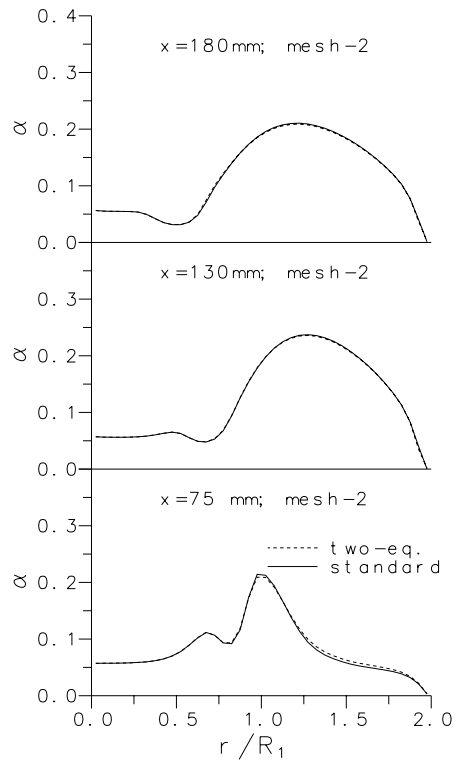

Figure 5 Effect on the predictions of the method used to obtain the volume fractions

In terms of robustness the various methods are applied to solve for α_c, instead of α_d, since in this way the more problematic bounding from above ($\alpha \leq 1$) can be assessed with this flow problem (due to the region where $\alpha_d = 0$). The results are summarised in Table 2 which gives the number of time steps to convergence (tolerances of 10^{-4} and 10^{-5}) and cpu times.

method	solve for:	mesh-1, tol=10^{-4}	mesh-1, tol=10^{-5}	mesh-3
standard, 3.2.1	α_d	698 (47.2)	815 (54.1)	3766 (8686)
	α_c	762 (60.0)	> 10000 (640)	> 10000
two-eq., 3.2.2	α_d	698 (49.1)	815 (56.2)	3767 (9166)
	α_c	698 (49.1)	815 (56.2)	3767 (9166)

Table 2.: Number of time steps and (CPU sec.) for convergence with the two bounding schemes for the sudden expansion

As expected, the two-equation method requires somewhat higher execution times compared with the existing (more 3.9% on the coarse mesh and 4.0% on the fine mesh). However, on the fine mesh it performs very well, converging in the same number of time

13

steps as the standard method when solving for α_d (when no upper bounding of α_d is necessary). The standard method fails to converge on the finer meshes when solving for α_c; the two-equation method on the other hand performs identically well since it solves for both α_c and α_d.

4.2 Flow Around Obstruction

In this problem a high void-fraction (inlet $\alpha = 40\%$), two-dimensional, turbulent, air/water mixture flows in the absence of gravity around a planar obstruction (blockage ratio $H_2/H = 5$, with half-width of obstruction $H = 10$ mm; see Fig. 6a). This flow resembles that around impeller blades where large zones of high void fraction are generated. The region in front of the obstruction ($x \leq 0$) is devoid of bubbles (high pressure region) and the region behind the obstruction ($x > 0$) has considerable bubble concentration but α is still far from 1 ($\alpha_{\text{maxi}} \approx 74\%$). Due to this, the matter of bounding α by 1 was studied indirectly by solving the equation for α_c (which is 1 at the start of the calculations, and is also 1 in the high-pressure region of the final steady-state solution, thus posing bounding problems).

Uniform inlet profiles for volume fraction ($\alpha_d = 0.4$) and velocity ($u_c = 2$m/s, $u_d = 2.2$ m/s) were imposed at the entrance plane at $x = -L_1$ ($L_1 = 250$mm). The thickness of the obstruction was 2mm and the region downstream was $L_2 = 500$ mm long. The absence of gravity leads to an increase in bubble concentration behind the obstacle.

Mesh	NC	$\delta x_{\min}/H$	$f_{x\text{-max}}$	$f_{y\text{-max}}$
1	3270	0.05	1.1295	1.0607
2	13080	0.025	1.0628	1.0299

Table 3.: Characteristics of meshes used for the obstruction problem
(NC-number of cells; f_x and f_y:expansion factors ($f_x \equiv \delta x_{i+1}/\delta x_i$)

Solution fields and mesh refinement- The meshes used are summarised in Table 3 and a portion of the fine mesh is given in Fig. 6 (a). The predicted fields obtained on mesh-2 are shown for void fraction in Fig. 6 (b), and turbulent kinetic energy (normalised with its maximum value, 0.370 m^2/s^2) in Fig. 6 (c), and mixture streamlines in Fig, 6 (d). The most striking feature is the zone in front of the obstacle where the void fraction falls sharply from 40% to zero. There is accumulation of bubbles behind the obstacle, in the recirculating zone which extends up to $X_R/H = 8.27$ and also in the area of high turbulence kinetic energy which develops in the shear layer behind the recirculation zone.

Several lateral profiles of void fraction are shown in Fig. 7 for the two computational meshes. More mesh refinement would be required for the profiles closer to the obstacle (namely at $x/H = 0.5$ and 1) to be less sensitive to the mesh, whereas those further downstream show little differences for the these two meshes.
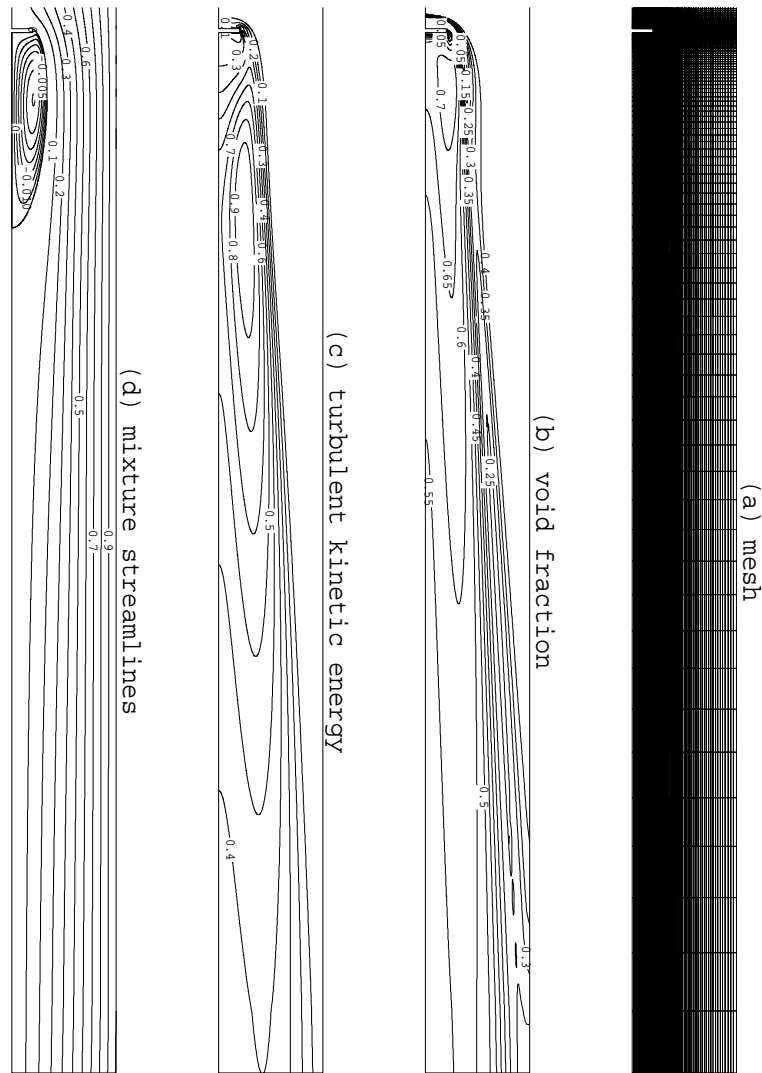
Figure 6 Predictions for the flow around an obstruction: (a) Mesh, (b) void fraction contours, (c) turbulent kinetic energy contours, and (d) mixture streamlines.

Bounding of volume fraction and equation used for α - The effect of the equation used to solve for α on the accuracy of the results can be seen from Fig. 8. This figure compares predictions of void fraction obtained with the standard (Eq. 20) and the two-equation (Eqs. 31-32) methods on the fine mesh, at two locations upstream of the contraction ($x/H = -0.5$ and -0, just upstream of the obstacle) and two locations downstream. No differences can be distinguished in the figure. A comparison of the α variation along the centreline also show a lack of effect, with both methods predicting an identical recirculating zone behind the obstruction, extending to a distance of $8.27H$.
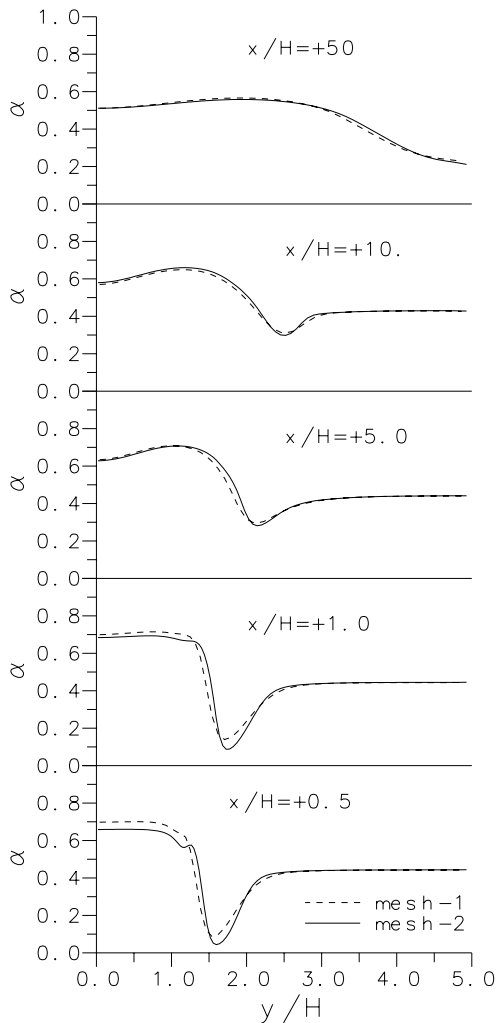
15

Figure 7 Effect of mesh refinement on the void fraction variations.
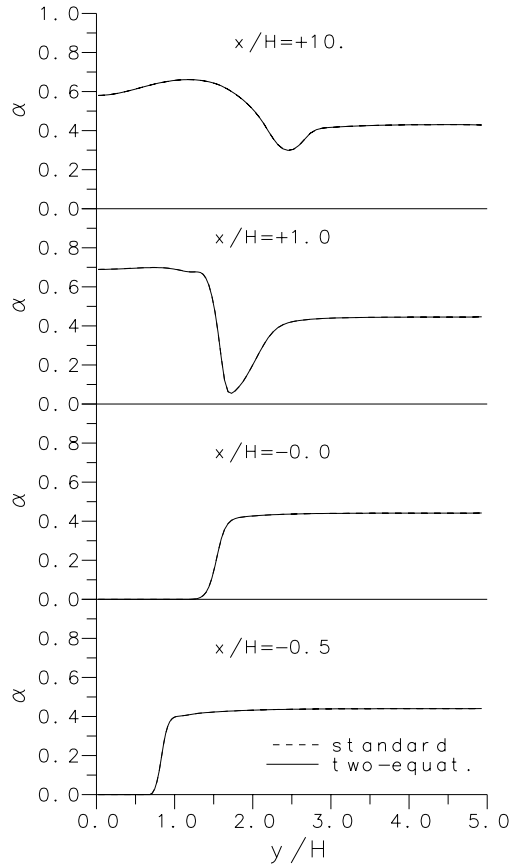

Figure 8 Effect of the equation solved for α on the predicted void fraction.

We examine now the relation between bounding method and robustness. The number of time steps for convergence (to a tolerance of 10^{-4}) are given in Table 4, as well as the corresponding CPU times in seconds (in a DEC-10000 machine). In all cases the time step was fixed at $\delta t = 5 \ 10^{-4}$ s which gives an approximate local Courant number of 3.1 on mesh-1 and 6.2 on mesh-2.

Table 4 shows that the standard method fails to converge on both meshes when solving for α_c. The two-equation method does very well on either mesh and its performance matches that of the standard method when the latter solves for α_d.

method	solve for:	mesh-1	mesh-1	mesh-2	mesh-2
		time steps	cpu (s)	time steps	cpu (s)
standard	α_d	3635	380	4230	2408
	α_c	> 10000	> 1060	diverge	-
two-equations	α_d	3615	345	4257	2547
	α_c	3615	345	4257	2547

Table 4. Number of time steps and cpu-time for convergence with the two bounding schemes (obstruction flow problem)

4.3 Phase stratification in a channel

The development of stratification of gas and liquid laminar flow is examined in a 2-D channel of width $H = 10$mm and length $L = 100$mm ($L/H = 10$). The density difference between the two phases was chosen to be small ($\rho_c = 1000$ kg/m^3 and $\rho_d = 950$ kg/m^3) so as to minimise numerical problems related to large discontinuities in pressure gradient at the interface. The other properties have been carefully chosen to guarantee adequate development of the flow from the inlet condition of the two equally mixed phases ($\alpha_d = 0.5$), to a complete stratification.

Solution fields and mesh refinement- Two uniform meshes with 50×20 and 100×40 cells have been utilised. The development of the lighter phase distribution is shown in Fig. 9 (using the modified α-equation). At the stations $x = 1$ and 2 H from inlet, the imposed inlet volume fraction of 0.5 is still seen in the central portion of the channel, but further downstream the two phases have fully separated with the heavier phase flowing at the bottom ($\alpha_d = 0$ for $y/H < 0.5$) and the lighter at the top ($\alpha_d = 1$ for $y/H > 0.5$). The slight over/undershoots of α in the first profiles are due to the problems arising from the Rhie-Chow interpolation.

The predictions in Fig. 9 are based on the finer mesh of 100×40 cells. With the coarser mesh (50×20 cells) the sharp interface between the regions of $\alpha_d = 0$ and 1 is less well
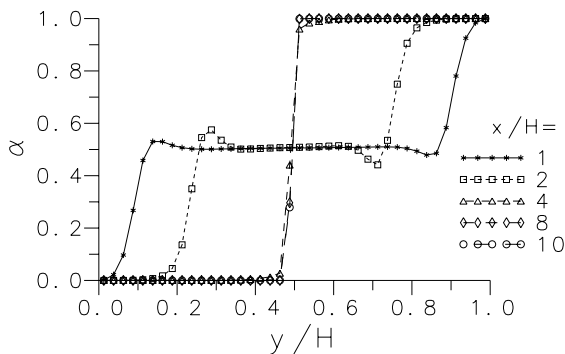
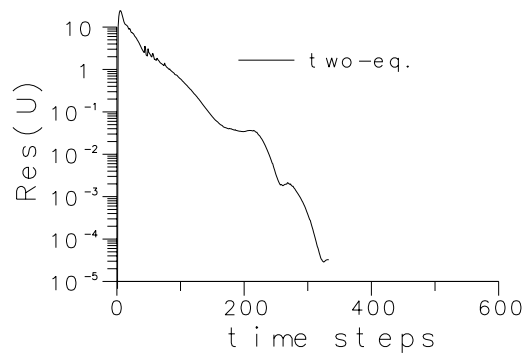Figure 9 Profiles of void fraction at several stations along the channel

Figure 10 Residuals history with two-equation method.

17

resolved, otherwise most other features are unchanged. For the profile near outlet ($x/H = 10$) the interface is resolved in 2 cells with the fine mesh.

Effect of bounding scheme - Fig. 10 shows convergence history for the u_c-momentum residuals. This shows good convergence behaviour, while the standard method fails altogether because of the effect of phase segregation.

5. CONCLUSIONS

The division of the momentum equations for each phase by the corresponding volume fraction seems to lead to better convergence characteristics of the two-phase flow algorithm. This improved numerical stability is retained with refinement of the computational meshes (very fine meshes were used in the 2-D test problems here presented). Some related *physical* issues should be further investigated (e.g., should the stress term in the equations be $\nabla \cdot \alpha \tau$ or $\alpha \nabla \cdot \tau$).

The two-equations bounding scheme, which solves the continuity equations for both phases, showed excellent overall behaviour easily coping with extreme cases of fully segregated phases.

References
[1] C.T. Crowe, M. Sommerfeld, Y. Tsuji, "Multiphase Flow with droplets and Particles", CRC Press (1998).
[2] R.I. Issa and P.J. Oliveira, "Numerical Prediction of Phase Separation in Two-Phase Flow Through T-Junctions", *Computers and Fluids*, **23**, 347-372 (1994).
[3] D.B. Spalding, "The Numerical Computation of Multi-phase Flows", CFDU, Imperial College, London, Report CFD/85/7 (1985).
[4] R.F. Kunz, B.W. Siebert, W.K. Cope, N.F. Foster, S.P. Antal, S.M. Ettorre, *Computers and Fluids*, 27, 741-768 (1998).
[5] J-C. Wu, K. Minemura, *Int. J. Numer. Meth. Fluids*, 29, 811-826 (1999).
[6] R.I. Issa and P.J. Oliveira, "Numerical Prediction of Turbulence Dispersion in Two-Phase Jet Flows", in *Two-Phase Flow Modelling and Experimentation 1995*, Ed. G.P. Celata and R.K. Shah, Edizioni ETS, Italy, 421-428 (1995).
[7] R.I. Issa and P.J. Oliveira, "Assessment of a Particle-Turbulence Interaction Model in Conjunction with an Eulerian Two-Phase Flow Formulation", in *Turbulence, Heat and Mass Transfer 2*, Ed. K. Hanjalić and T.W.J. Peeters, Delft Univ. Press, 759-770 (1997).
[8] S.V. Patankar, "Numerical Heat Transfer and Fluid Flow", Hemisphere Pub. (1980).
[9] P.J. Oliveira, PhD thesis, Imperial College (1992).
[10] M.B. Carver, "A Method of Limiting Intermediate Values of Volume Fraction in Iterative Two Fluid Computations", *J Mech. Engng. Science*, 24, 221-224 (1982)
[11] R. Bel Fdhila and O. Simonin, "Eulerian Prediction of a Turbulent Bubbly Flow Downstream of a Sudden Pipe Expansion", Proc. 6*th Workshop on Two Phase Flow Predictions.* Erlangen. Ed. M. Sommerfeld (1992) .